Inner Solar System Material Discovered in the Oort Cloud

Karen J. Meech[1,], Bin Yang[,2], Jan Kleyna[1], Olivier R. Hainaut[,3], Svetlana Berdyugina[1,4], Jacqueline V. Keane[3], Marco Micheli[5-7], Alessandro Morbidelli[8], Richard J. Wainscoat[1]

Teaser: Fresh inner solar system material preserved in the Oort cloud may hold the key to understanding our solar system formation

[1]Institute for Astronomy, University of Hawai'i, 2680 Woodlawn Drive, Honolulu, Hawaii 96822-1839, USA.

[2]European Southern Observatory, Alonso de Cordova 3107, Vitacura, Casilla 19001, Santiago, Chile

[3]European Southern Observatory, Karl-Schwarzschild-Strasse 2, 85748 Garching bei Munchen, Germany

[4]Kiepenheuer Institut fuer Sonnenphysik, Schoeneckstrasse 6, 79104 Freiburg, Germany

[5]SSA NEO Coordination Centre, European Space Agency, 00044 Frascati (RM), Italy

[6]SpaceDyS s.r.l., 56023 Cascina (Pl), Italy

[7]INAF-IAPS, 00133 Roma (RM), Italy

[8]Laboratoire Lagrange, UMR7293, Universite de Nice Sophia-Antipolis, CNRS, Obs. de la Cote d'Azur, Boulevard de l'Observatoire, 06304 Nice Cedex 4, France

Manuscript submitted to *Science Advances:*

Revised, 2016-02-28

Total pages including abstract, text, references, table and figures captions: 21
Total words (abstract): 200
Total words (body text): 2692
Total References for paper + supplement: 56

We have observed C/2014 S3 (PANSTARRS), a recently discovered object on a cometary orbit coming from the Oort cloud that is physically similar to an inner main belt rocky S-type asteroid. Recent dynamical models succeed in reproducing key characteristics of our current solar system; some of these models require significant migration of the giant planets, while others do not. These models provide different predictions on the presence of rocky material expelled from the inner Solar System in the Oort cloud. C/2014 S3 could be the key to verifying these predictions of the migration-based dynamical models. Furthermore, this object displays a very faint, weak level of comet-like activity, five to six orders of magnitude less than typical ice-rich comets on similar orbits coming from the Oort cloud. Various arguments convince us that this activity is produced by sublimation of volatile ice, *i.e.* normal cometary activity. The activity implies that C/2014 S3 has retained a tiny fraction of the water that is expected to be present at its formation distance in the inner solar system. We may be looking at fresh inner solar system Earth-forming material, ejected from the inner solar system and preserved for billions of years in the Oort cloud.

Introduction

Small primitive bodies were witness to the solar system's formative processes. When gas was present in the disk, during the first 5 million years of the solar system formation, a local chemical signature was imprinted on the planetesimals. The connection to today's solar system relies on how this material was dynamically re-distributed during the planet forming process. To connect early planet formation to the modern era, compositions of a range of primitive bodies from different locations in the solar system must be measured and compared with the predictions from early solar system formation models, some of which predict significant reshuffling of material throughout the solar system. Ground- and space-based observations of comets have played a key role in mapping out early solar system chemistry, and observations of protoplanetary disks are now generating chemical maps of other forming planetary systems to use as constraints of disk chemical models.

There are now several dynamical models that can reproduce much of our solar system's current architecture. The “Grand Tack” model (*1*) starts the solar system formation simulation at an early phase when the giant planets grew and migrated in a gas-rich protoplanetary disk. During their inward migration, the giant planets scattered inner solar system material outward; during their outward migration they implanted a significant amount of icy planetesimals from 3.5-13 AU into the inner solar system. The Grand Tack model predicts the presence of rocky objects in the Oort cloud in a ratio of icy comets to rocky asteroids of 500-1000 to one (*2*). Other dynamical models, which assume non-migrating giant planets, make different predictions about the fraction of the Oort cloud population comprising planetesimals initially within the asteroid belt or the terrestrial planet region. These predictions range from 200 to 2000 to one (*3-4*). Other models do not explicitly estimate the mass of rocky planetesimals eventually implanted in the Oort cloud (*5*), but from the initial available amount it is legitimate to expect that the ratio of icy to rocky planetesimals in the final Oort cloud is 200-400. Instead, a recent radically different model of terrestrial planet formation predicts that the planetesimals in the inner solar system always had a negligible total mass (*6*); in this case there would be virtually no rocky Oort cloud population.

The discovery and characterization of a rocky object from the Oort cloud is therefore the first step toward measuring the fraction of rocky objects in the Oort cloud. This will provide strong constraints for the models.

Materials and Methods

On 2014 September 22, the Pan-STARRS1 telescope discovered a weakly active comet at a heliocentric distance of 2.1 AU, designated C/2014 S3 (PANSTARRS) (hereafter C/2014 S3). C/2014 S3 has a long-period comet orbit (semi major axis = 90.5 AU, eccentricity = 0.977, perihelion = 2.049 AU, aphelion = 178.9 AU, inclination=169.3^{o}, period= 860.3 yr), whose source reservoir is most likely the Oort cloud (*7*). Because of the nearly tailless appearance at a distance where long-period comets are very active, the object has been called a "Manx" comet, after the tailless cat. Observations in the days following the discovery suggested that its colors might be interesting, so follow up multi-filter observations were obtained on 2014 October 22 and 24 on the Canada-France-Hawaii Telescope (CFHT), and spectra were acquired on 2014 November 18 using the Very Large Telescope (VLT) in Chile. Images of C/2014 S3 are shown in Fig. 1 and the reflectivity spectrum is shown in Fig. 2 (*2*).

The overall shape of the spectrum, and in particular the 1 μm dip in the spectral reflectivity of C/2014 S3 shows that the surface is consistent with S-type asteroids, found typically in the inner asteroid main belt; the spectrum is inconsistent with all other minor body surfaces: typical comets, trans-Neptunian objects, and asteroids of all other classes. Comets (and trans-Neptunian objects, a reservoir from which a class of comets comes from) are believed to have formed in the outer solar system, and their wide range of neutral to red colors reflect a mix of organics, ice and surface weathering processes. Moderately red S-type bodies, on the other hand are believed to have formed relatively dry in the inner solar system (*8*).

C/2014 S3 was observed with a dust coma at 2.1 and 2.2 AU (see Fig. 1). By 2.3 AU, the activity had decreased, but a small coma was still visible. To test whether the dust coma is caused by volatile outgassing or by a collision, we have constructed a simple water-ice sublimation model (*2*). We do not have enough data to fully constrain an ice sublimation model, but the data are consistent with the behavior expected of dust dragged from the nucleus by sublimating water ice (Fig. 3). We ran two models, one assuming typical icy comet characteristics (albedo of 4%), and one assuming typical S-type reflectivity (25%). The S-type model provides a better match to the data. In both cases, the implied nucleus is small, with a radius between 0.7 to 0.25 km, respectively. The implied gas production rate at perihelion is low, between 3×10^{23} to 1×10^{24} molecules/s, equivalent to a sublimating patch of pure ice 10 to 30 m in radius and five to six orders of magnitude lower than typical Oort cloud comets at the same heliocentric distance.

The appearance of the dust coma is also more consistent with continuous activity than with an impact. The coma extends far outside the syndyne and synchrone envelope (which describes the locus of dust grains of different sizes, emitted from the nucleus with zero velocity at different times, accounting for the solar gravity and radiation pressure; (*2*), in particular to the south and to the southwest in the September and October images, respectively (as shown in Fig. 1). This indicates that the dust was ejected with a moderate, but non-zero velocity. At the heliocentric distance of C/2014 S3, the grains

should be lifted off the surface by a tenuous gas flow with a velocity of 730 m/s (*11*). A distribution of velocities in amplitude and direction, as expected for a sublimating body, will result in a blurring of the syndyne and synchrone pattern as observed.

In the region covered by the synchrones and syndynes, the dust extends over a wide range of synchrones, suggesting a wide range of emission times, although the timestamps are approximate because of the initial velocity of the dust. In the competing hypothesis of a high-velocity impact on a small body with weak self-gravitation, ejecta are expected to be launched in a characteristic ejection cone. After some days or weeks, this cone results in a very distinct coma. Such a case was modeled in detail for another body of similar size at similar distance showing a wide range of resulting coma features (*12*). While the variety of possible collision geometries is enormous, the most salient features in the dust cloud are always parallel to the synchrone corresponding to the time of the impact. This reflects the fact that the impulsive dust emission releases a full distribution of dust grain sizes at a single epoch. The fact that the coma of C/2014 S3 does not have any preferential direction indicates that the emission was not impulsive, as it would be in an impact.

We calculated the probability of an impact on C/2014 S3 with a meter-sized object or larger on its current orbit while crossing the asteroid belt. This is done considering the number density of m-size asteroids in the asteroid belt volume (3.9×10^{-14} km^{-3}), the physical radius of C/2014 S3 (0.7 km) and its relative speed while crossing the belt (42 km/s). The probability of a collision before we observed C/2014 S3 is 5×10^{-5}. Thus it is very unlikely that the dust coma is caused by an impact. Some inner main belt asteroids are suspected to shed dust because they have been spun up to their critical rotation periods by radiation pressure effects. This does not apply to C/2014 S3, which spent most of its orbit far from the Sun. Overall, we are therefore confident that the coma is produced by sublimation.

We estimate that in today's solar system, there are about 200 km-size S-type asteroids escaping from the main asteroid belt per million years (*13*). Approximately 20 of these are scattered by Jupiter, and of these, about 1 passes through the Oort cloud and could be re-injected inwards on a Manx orbit. This would amount to only 0.4 returning objects per million years, thus it is unlikely that we will observe this contamination. C/2014 S3 is not such an object because it is active, whereas today's S-type asteroids are not.

Implications of an Active S-type Object from the Oort Cloud

When Oort formulated his model of the Oort cloud (*14*), he inferred that there were too few comets that were on their return passage through the solar system. He proposed that the comets faded due to physical evolution and volatile loss. However, it is expected that volatiles in ice-rich bodies should be able to sustain cometary activity for up to 1000 perihelion passages (*4*). Further, models for the number of Oort cloud comets entering the inner solar system that subsequently fade predict a large number of dormant isotropic long-period comets that are not seen (*15*). Thus, the majority of Oort cloud comets must be lost because they physically disrupt, not because they become inactive due to volatile loss. Nevertheless, it cannot be excluded that some comets become inactive. The point is that inactive comets should have a D- or P-type spectrum, not have an S-type reflectivity (16). Accordingly, we can conclude at C/2014 S3 is not an almost extinct comet.

C/2014 S3 is not the first nearly inactive object on a long-period comet orbit to be found. The first, discovered by the Near-Earth Asteroid Tracking (NEAT) search, was 1996 PW (*17*). 1996 PW generated only moderate attention observationally, with observations indicating it was not active, red, had a radius between 4-8 km, and was a slow rotator. An exploration of the dynamical history of 1996 PW to assess whether it was an extinct Oort cloud comet, an Oort cloud asteroid, or something more recently ejected outward such as an extinct ecliptic comet or a main belt asteroid showed that it was equally probable that 1996 PW was an extinct comet or an asteroid ejected into the Oort cloud during the early evolution of the Solar System (*4*). More recently, other Manx candidates have been discovered. We have observed five of them, which also show comet-like red colors like 1996 PW. C/2014 S3 is the first and only Manx to date with an S-type reflectivity spectrum.

What are the implications of seeing low-level potentially volatile-driven activity from an object with an S-type spectrum on a returning long-period comet from the Oort cloud? There is widespread evidence for aqueous alteration throughout primitive asteroids originating in the outer asteroid belt (*18-19*). There is also evidence that water may still be present in the outer asteroid main belt—observable as outgassing from main belt comets (*20*) and dwarf planets (*21*), or as ice on the surfaces of asteroids (*22*).

S-type asteroids, which are dominant in the inner main asteroid belt today and formed from inner solar system material, are clearly inactive and are neither expected nor observed to possess ices (*8*). Cosmochemical studies of meteorites have shown that many classes of meteorites underwent extensive aqueous processing in their parent bodies. The hydrated C and D type asteroids are commonly associated with carbonaceous chondrite meteorites (23), but the best match between meteorite classes and the S-type asteroids comes from the ordinary chondrites (OC). This was confirmed with Hayabusa mission samples returned from the S-type asteroid Itokawa (*24-25*).

The 1 μm and 2 μm absorption bands in the near-IR (NIR) and the visible-NIR spectral slope are used to interpret surface mineralogies of S-type asteroids. The relative band centers and depths can be used to assess the relative abundance of olivine-pyroxene, and the Fe^{2+} and Ca^{2+} contents in these minerals. The spectral slope in the 1-2 μm region is related to the FeNi metal content and olivine abundance (*26*). The wide range of S-type mineralogical variations have been divided into sub-classes with the S(IV) class being the one that matches C/2014 S3 the best (Fig. 2). Interestingly, the S(IV) class most likely represents the parent bodies of the OC meteorites. The silicates (olivine and pyroxene) inferred for the S(IV) asteroids are similar to unequilibrated ordinary chondrites (UOCs) (*26*). The UOCs are the most primitive of the OCs, never reaching very high temperatures (*27*). The UOCs have olivine / (olivine+low-calcium pyroxene) ratios which are manifested in a very shallow 1-μm band similar to that seen in (3) Juno and (7) Iris (*28*). The surface of C/2014 S3 appears to be consistent with more primitive S-type material.

Chondrite accretion ages and the conditions under which they were aqueously altered can be used to constrain where they accreted. Previously, because of the absence of carbonates in ordinary chondrites and the lack of proper standards, there had been no reliable ages for aqueous activity for OC parent bodies. New work on an L3 chondrite (one of the most pristine OCs) has now shown the

presence of fayalite, a secondary mineral that is a product of aqueous alteration (*29*). The mineralogy and thermodynamic analysis of the sample showed that the fayalite was consistent with formation at low temperatures and a low water-rock mass ratio (0.1-0.2); much lower than measured values in comets (*30*). Accretion ages between 1.8-2.5 Myr after the formation of the first solar system solids for the L-parent bodies and the ages at which the aqueous secondary minerals formed suggest that some water ice was incorporated into the accreting parent bodies, and that they accreted close to the protoplanetary disk snowline (*29*). The snowline likely varied in position over time, but many models suggest that, towards the end of the protoplanetary disk phase, it could have been within the terrestrial planet forming region (*31*). This is close to where it is believed the ordinary chondrite parent bodies accreted. While the minerals in the OCs are anhydrous and formed under dry conditions, it is possible that they could have acquired some water later.

These observations may tie together other reported observations that appeared to contradict the current understanding of solar system formation. There was clear evidence in the comet dust samples from the *Stardust* mission that there had been substantial radial migration in the protoplanetary disk, with comet dust having seen regions of high temperature (*32*). Fluid water inclusions have been found in the Monahans OC, and one possible explanation for this was that water was exogenously delivered after it formed (*33*). The Orgueil meteorite has long been considered a candidate for a possible cometary origin, or from a body rich in volatiles (*34*). The discovery that C/2014 S3, an object on a cometary orbit that has the characteristics of an inner solar system asteroid, can offer new ideas about the relation between meteorites and their sources.

C/2014 S3 has an orbit typical of that of a returning Oort cloud comet. Our analysis of the activity of C/2014 S3 suggests that the dust coma is consistent with sublimation. The level of activity is five to six orders of magnitude lower than active long-period comets at a similar distance. The spectrum of C/2014 S3 is consistent with S-type asteroidal material and the location and depth of the 1-μm band suggests that the material may be minimally thermally processed. This presents the intriguing possibility that we are seeing relatively fresh inner solar system material that has been stored in the Oort cloud and is now making its way into the inner solar system. Many dynamical models make predictions about the amount of inner solar system material that could reside in the Oort cloud as a result of scattering by the giant planets, and these predictions radically differ depending on the initial mass of the asteroid population that these models assume/imply. Assessing how many S-type objects exist will be a strong test of these models. To unambiguously select between dynamical models, 50-100 Manx objects need to be characterized; the number of S-types found will distinguish between the models (*2*).

References

1. K.J. Walsh, A. Morbidelli, S.N. Raymond, D.P. O'Brien, A,M. Mandell, A low mass for Mars from Jupiter's early gas-driven migration'', *Nature* **475**, 206-209 (2011). doi:10.1038/nature10201

2. These issues are treated at greater length (including discussion of observations and data reduction) in the supporting material on *Science Advances* Online.

3. A. Shannon, A.P. Jackson, D. Veres, M. Wyatt, Eight billion asteroids in the Oort cloud, *Mon. Not. R. Astron. Soc.* **446**, 2059-2064 (2015). doi:10.1093/mnras/stu2267

4. P. Weissman, H.F. Levison, Origin and evolution of the unusual object 1996 PW: Asteroids from the Oort Cloud? *Astrophys. J.* **488**, L133-L136 (1997). doi:10.1086/310940

5. A. Izidoro, K. de Souza Torres, O.C. Winter, N. Haghighipour, A compound model for the origin of Earth's water, *Astrophys. J.* **767**, id. 54 (2013). doi:10.1088/0004-637X/767/1/54

6. H.F. Levison, K.A. Kretke, M.J. Duncan, Growing the gas-giant planets by the gradual accumulation of pebbles, *Nature* **524**, 322-324 (2015). doi:10.1038/nature14675

7. L. Dones, R. Brasser, N. Kaib, H. Rickman, Origin and evolution of the cometary reservoirs, *Space Sci. Rev.* **197**, 191-269 (2015) doi:10.1007/s11214-015-0223-2

8. S-type asteroids, which have been associated with ordinary chondrites, are generally expected to be dry. Type 4-6 ordinary chondrites consist of anhydrous minerals and their mineral assemblages reflect dry thermal metamorphism (*9*). However, some type 3 ordinary chondrites have experienced aqueous alteration that has converted matrix minerals and some chondrule glass to hydrous phases (*9,10*). The general expectation is that the type 3 chondrites come from near the surface of the parent asteroid where metamorphic temperatures were the lowest. It is not clear that we have samples of the true asteroid surface because that material may not be tough enough to survive passage through space and through the atmosphere to reach earth. So the presence of a tail on object C/2014 S3 and the indication of hydrated silicates in the spectrum are not entirely inconsistent with this object being chondritic.

9. G.R. Huss, A.E. Rubin, J.N. Grossman, Thermal metamorphism in chondrites, in *Meteorites and the Early Solar System II*, D.S. Lauretta and H.Y. McSween, Jr, editors, 567-586 (2006).

10. M.K. Weisberg, T.J. McCoy, A.N. Krot, Systematics and evaluation of meteorite classification., in *Meteorites and the Early Solar System II*, D.S. Lauretta and H.Y. McSween, Jr, editors, 19-52 (2006).

11. N.T. Bobrovnikoff, Physical properties of comets, *Astron. J.* **59**, 357-358 (1954).

12. J. Kleyna, O.R. Hainaut, K.J. Meech, P/2010 A2 LINEAR. II. Dynamical dust modelling, *Astron. Astrophys.* **549**, id. A13 14 pp. (2013). doi:10.1051/0004-6361/201118428

13. W.F. Bottke, A. Morbidelli, R. Jedicke, J.-M. Petit, H.F. Levison, P. Michel, T.S. Metcalfe, Debiased orbital and absolute magnitude distribution of the near-earth objects, *Icarus* **156**, 399-433, (2002). doi:10.1006/icar.2001.6788

14. J.H. Oort, The structure of the cloud of comets surrounding the solar system and a hypothesis concerning its origin, *Bull. Astron. Inst. Neth.* **11**, 91-110 (1950).

15. H.F. Levison, A. Morbidelli, L. Dones, R. Jedicke, P.A. Wiegert, W.F. Bottke, The mass misruption of Oort cloud comets, *Science* **296**, 2212-2215 (2002). doi:10.1126/science.1070226

16. P.R. Weissman, W.F. Bottke, H.F. Levison, Evolution of comets into asteroids, in *Asteroids III*, W.F. Bottke, Jr., A.Cellino, P. Paolicchi, R.P. Binzel, editors, Univ. AZ Press, Tucson, p. 669-686.

17. E.F. Helin, S. Pravdo, K.J. Lawrence, 1996 PW, MPEC 1996-P03 (1996).

18. A.J. Brearley, The action of water, in *Meteorites and the Early Solar System II*, Lauretta, D.S. McSween, H.Y., Eds., Univ. AZ Press, Tucson, pp. 584-624 (2006).

19. A.N. Krot, I.D. Hutcheon, A.J. Brearley, O.V. Pravdivtseva, M.I. Petaev, C.M. Hohenberg, Timescales and settings for alteration of chondritic meteorites, in *Meteorites and the Early Solar System II*, D.S. Lauretta, H.Y. McSween, Eds., Univ. AZ Press, Tucson, pp. 525-553 (2006).

20. H. Hsieh, D. Jewitt, D., A population of comets in the main asteroid belt, *Science* 312, 561-563 (2006). doi:10.1126/science.1125150

21. M. Kuppers, L. O'Rourke, D. Bockelee-Morvan, V. Zakharov, S. Lee, S., *et al.*, Localized sources of water vapour on the dwarf planet (1) Ceres, *Nature* **505**, 525-527 (2014). doi:10.1038/nature12918

22. H. Campins, K. Hargrove, N. Pinilla-Alonso, E.S. Howell, M.S. Kelley, *et al.*, Water ice and organics on the surface of the asteroid 24 Themis, *Nature* **464**, 1320-1321 (2010). doi:10.1038/nature09029

23. T.H. Burbine, T. J. McCoy, A. Meibom, B. Gladman, K. Keil, Meteoritic Parent Bodies: Their Number and Identification. in *Asteroids III*, W.F. Bottke, A. Cellino, P. Paolicchi, R.P. Binzel, Eds., Univ. Arizona Press, Tucson, p. 653-667.

24. T. Mikouchi, M. Komatsu, K. Hagiya, K. Ohsumi, M. Zolensky *et al.*, Mineralogy and crystallography of some Itokawa particles returned by the Hayabusa asteroidal sample return mission, *Earth, Planets Space* **66**, id. 82, 9 pp (2014). doi:10.1186/1880-5981-66-82

25. T. Nakamura, T. Noguchi, M. Tanaka, M.E. Zolensky, M. Kimura *et al.,* Itokawa dust particles: A direct link between S-Type asteroids and ordinary chondrites. *Science* **333**, 1113-1116 (2011). doi:10.1126/science.1207758

26. M.J. Gaffey, J.F. Bell, J.F., R.H. Brown, Mineralogical variations within the S-type asteroid class, *Icarus* **106**, 573-602 (1993). doi:10.1006/icar.1993.1194

27. G.R. Huss, A.E. Rubin, J.N. Grossman, Thermal metamorphism in chondrites, in *Meteorites and the Early Solar System II*, D.S. Lauretta, H.Y. McSween Jr., Eds., Univ. AZ Press, Tucson, pp. 567-586.

28. P. Vernazza, B. Zanda, R.P. Binzel, T. Hiroi, F.E. DeMeo, *et al.*, Multiple and fast: The accretion of ordinary chondrite parent bodies, *Astroph. J.* **791**, id. 120, 22 pp. (2014). doi:10.1088/0004-637X/791/2/120

29. P.M. Doyle, K. Jogo, K. Nagashima, A.N. Krot, Early aqueous activity on the ordinary and carbonaceous chondrite parent bodies recorded by fayalite, *Nature Communications* **6**, 7444 (2015). doi:10.1038/ncoms8444

30. A. Rotundi, H. Sierks, V. Della Corte, M. Fulle, P.J. Gutierrez *et al.*, Dust measurements in the coma of comet 67P/Churyumov-Gerasimenko inbound to the Sun, *Science* **347**, aaa3905 (2015). doi:10.1126/science.aaa3905

31. K. Baillie, S. Charnoz, E. Pantin, Time evolution of snow regions and planet traps in an evolving protoplanetary disk. *Astron. Astrophys.* **577**, id. A65, 12pp (2015). doi:10.1051/0004-6361/201424987

32. M.E. Zolensky, T.J. Zega, H. Yano, S. Wirick, A. Westphal, A. *et al.,* Mineralogy and petrology of Comet 81P/Wild 2 nucleus samples, *Science* **314**, 1735 (2006). doi:10.1126/science.1135842

33. M.E. Zolensky, R.J. Bodnar, K.E. Gibson, L.E. Nyquist, Y. Reese *et al.*, Asteroidal water within fluid inclusion-bearing halite in an H5 chondrite, Monahans, *Science* **285**, 1377-1379. doi:10.1126/science.285.5432.1377

34. M. Gounelle, M.E. Zolensky, The Orgueil meteorite: 150 years of history, *Met. Plan. Sci.* **49**, 1769-1794 (2014). doi:10.1111/maps.12351.

35. S.J. Bus, R.P. Binzel, Phase II of the Small Main-Belt Asteroid Spectroscopic Survey: The observations, *Icarus* **158**, 106-145 (2002). doi:10.1006/icar.2002.6857

36. M. Fukugita, T. Ichikawa, J.E. Gunn, M. Doi, K. Shimasaku, D.P. Schneider, The Sloan digital sky survey photometric system, *Astron. J.* **111**, 1748-1756 (1996). doi:10.1086/117915.

37. E.A. Magnier, E. Schlafly, D. Finkbeiner, M. Juric, J.L. Tonry *et al.*, The Pan-STARRS 1 photometric reference ladder, release 12.01, *Astrophys. J. Supp.*, **205**, id. 20, 13 pp. (2013). doi:10.1088/0067-0049/205/2/20.

38. J.L. Tonry, C.W. Stubbs, K.R. Lykke, P. Doherty, I.S. Shivvers *et al.*, The Pan-STARRS 1 photometric system, *Astrophys. J.*, **750**, id. 99, 14 pp. (2012). doi:10.1088/0004-637X/750/2/99

39. E. Bertin, S. Arnouts, SExtractor: Software for source extraction, *Astron. Astrophys. Supp*., **317**, 393-404 (1996). doi:10.1051/aas:1996164

40. Transformations between the Sloan Survey photometric system and other standard systems are found on the Sloan Digital Sky Survey website: http://classic.sdss.org/dr4/algorithms/sdssUBVRITransform.html

41. F. Masset, M. Snellgrove, Reversing type II migration: resonance trapping of a lighter giant protoplanet, *Mon. Not. Roy, Astr. Soc.*, **320**, L55-L59 (2001). doi: 10.1046/j.1365-8711.2001.04159.x

42. K. Tsiganis, R. Gomes, A. Morbidelli, H.F. Levison, Origin of the orbital architecture of the giant planets of the solar system, *Nature* **435**, 459-461 (2005). doi:10.1038/nature03539

43. R. Brasser, A. Morbidelli, Oort Cloud and Scattered disc formation during a late dynamical instability in the solar system, *Asteroids, Comets, Meteors 2012, LPI Contribution No. 1667*, id.6005

44. R. Brasser, M.J. Duncan, H.F. Levison, Embedded star clusters and the formation of the Oort Cloud, *Icarus* **184**, 59-82 (2006). doi:10.1016/j.icarus.2006.04.010

45. R. Brasser, M.E. Schwamb, Re-assessing the formation of the inner Oort cloud in an embedded star cluster-II. Probing the inner edge, *Mon. Not. Roy. Astron. Soc.* **446**, 3788-3796 (2015). doi:10.1093/mnras/stu2374

46. C. Hayashi, Structure of the solar nebula, growth and decay of magnetic fields and effects of magnetic and turbulent viscosities on the nebula, *Prog. Theor. Phys. Suppl.* **70**, 35-53 (1981).

47. R.J. Walker, Highly siderophile elements in the Earth, Moon and Mars: Update and implications for planetary accretion and differentiation, *Chemie der Erde, Geochem.* **69**, 101-125 (2009). doi:10.1016/j.chemer.2008.10.001

48. L. Dones, P.R. Weissman, H.F. Levison, M.J. Duncan, Oort cloud formation and dynamics, in *Comets II*, M.C. Festou, H.U. Keller, H.A. Weaver (eds). Univ. AZ Press, Tucson, 153-174 (2004).

49. M. Lambrechts, A. Johansen, Rapid growth of gas-giant cores by pebble accretion, *Astron. Astrophys.* **544**, id. A32 (2012). doi:10.1051/0004-6361/201219127

50. B.M.S. Hansen, Formation of the terrestrial planets from a narrow annulus, *Astrophys. J.* **703**, 1131-1140 (2009). doi:10.1088/0004-637X/703/1/1131

51. K.J. Meech, D. Jewitt, G.R. Ricker, Early photometry of comet P/Halley - development of the coma, *Icarus* **66**, 561-574 (1986). doi:10.1016/0019-1035(86)90091-6

52. C. Snodgrass, C. Tubiana, D.M. Bramich, K. Meech, H. Boehnhardt, L. Barrera, Beginning of activity in 67P/Churyumov-Gerasimenko and predictions for 2014-2015, *Astron. Astrophys.*, **557**, id. A33, 15 pp. (2013). doi:10.1051/0004-6361/20132020

53. N. Fray, B. Schmitt, B. Sublimation of ices of astrophysical interest: A bibliographic review, *Plan. Space Sci.*, **57**, 2053-2080 (2009). Doi:10.1016/j.pss.2009.09.011

54. O. Groussin, J.M. Sunshine, L.M. Feaga, L. Jorda, P.C. Thomas *et al.* The temperature, thermal inertia, roughness and color of the nuclei of Comets 109P/Hartley 2 and 9P/Tempel 1, *Icarus* **222**, 580-594 (2013). doi:10.1016/j.icarus.2012.10.003

55. M.L. Finson, E.F. Probstein, A theory of dust comets. I. Model and equations, *Astrophys. J.*, **154**, 327-352 (1968). doi:10.1086/149761

56. D.T. Britt, D. Yeomans, K. Housen, G. Consolmagno, Asteroid density, porosity, and structure, in *Asteroids III*, W.F. Bottke, Jr., A. Cellino, P. Paolicchi, R.P. Binzel, Eds., Univ. AZ Press, Tucson, 485-500 (2002).

57. P. Wiegert, S. Tremaine, The evolution of long-period comets, *Icarus* **137**, 84-121 (1999). doi:10.1006/icar.1998.6040

Supplementary Materials Supplementary material for this article is available.

Acknowledgements Based on observations obtained with the CFHT (programs 14bh07 and 14bh27) and ESO under program 294.C-5009(A). Given that the comet was rapidly fading, we are greatful to the ESO Director General for swiftly approving our DDT request (within 5 hours of receipt of the proposal) given that the comet was rapidly fading. It was this rapid turn around that made this observation possible. We also thank the exceptional UT1 science operations staff, and Ferdinando Patat, who managed to get the program into the queue within 48 hours of the proposal submission. **Funding:** K.J.M., J.V.K. and J.K. acknowledge support through the NASA Astrobiology Institute, and partial support through NASA grant NNX13A151G, and NSF grant AST1413736. S.B. acknowledges support through an ERC Advanced grant HotMol ERC-2011-AdG-291659 and R.J.W. acknowledges support by NASA under grants NNX12AR65G and NNX14AM74G. A.M. acknowledges support by the French ANR, project number ANR-13-13-BS05-0003-01 project MOJO (Modeling the Origin of JOvian planets). We also thank Gary Huss for useful discussions. **Competing interests:** The authors declare that they have no competing interests. **Data and materials availability:** All data needed to evaluate the conclusions in the paper are present in the paper, the supplementary materials, and through the following data archives: (1) the VLT data are accessible through the ESO Science Archive Facility at http://archive.eso.org/cms.html, and (2) the CFHT data are accessible through the Canadian Astronomy Data Centre at http://www.cadc-ccda.hia-iha.nrc-cnrc.gc.ca/en/.

Author Contributions K.J.M conceived of the project, secured the telescope time and developed the sublimation models. R.J.W. alerted the team to the PS1 discovery and obtained some of the imaging observations. M.M. performed the astrometry and searched for additional images in the Pan-STARRS1 database. O.R.H. prepared the observations for the VLT, and B.Y. carried out the observations. B.Y., S.B. and O.R.H. performed the spectral reductions. J.K. prepared the imaging observations, and did the photometric reductions. J.V.K. contributed to the analysis and interpretation of the data. A.M. provided the dynamical discussion, and calculated the impact probabilities.

Author Information Correspondence and requests for materials should be addressed to K.J.M. (meech@ifa.hawaii.edu).

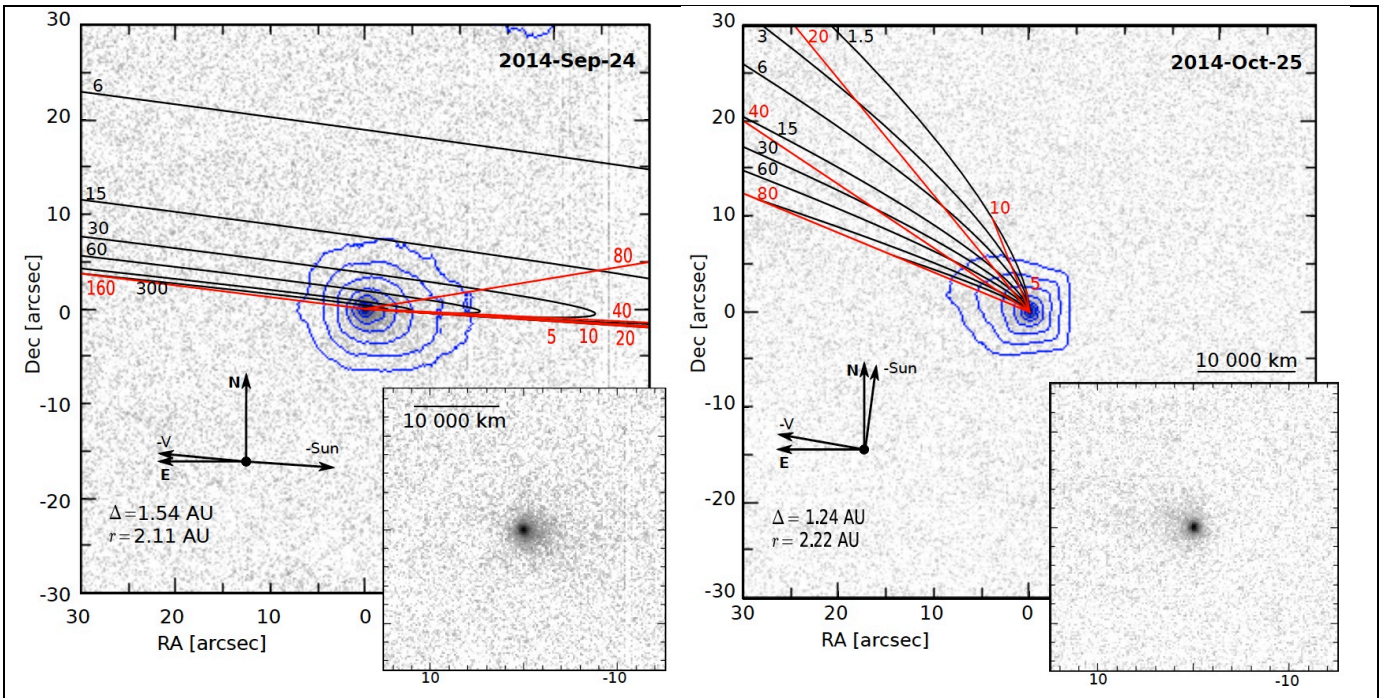

Figure 1. Images of C/2014 S3 (PANSTARRS) obtained on 2014 September 24 (left) and October 25 (right) with the Canada-France-Hawaii Telescope. The background stars have been processed out of these composites. The comet was at heliocentric distances of 2.11 and 2.22 AU, moving outward from its perihelion at 2.05 AU on 2014 August 13. The syndynes (black; grain sizes are in μm) and synchrones (red; positions noted in days, prior to the observations) map out the expected position of the dust released from the nucleus under the influence of solar radiation pressure. Different lines indicate the locus of dust of different sizes released at different times; the dramatic change between the two epochs reflects very different viewing geometries. The blue isophotes are equally spaced on a logarithmic scale. The insets are at the same scale as the main images. The arrows indicate the directions of North and East and of the anti-solar and negative of the heliocentric velocity vectors.

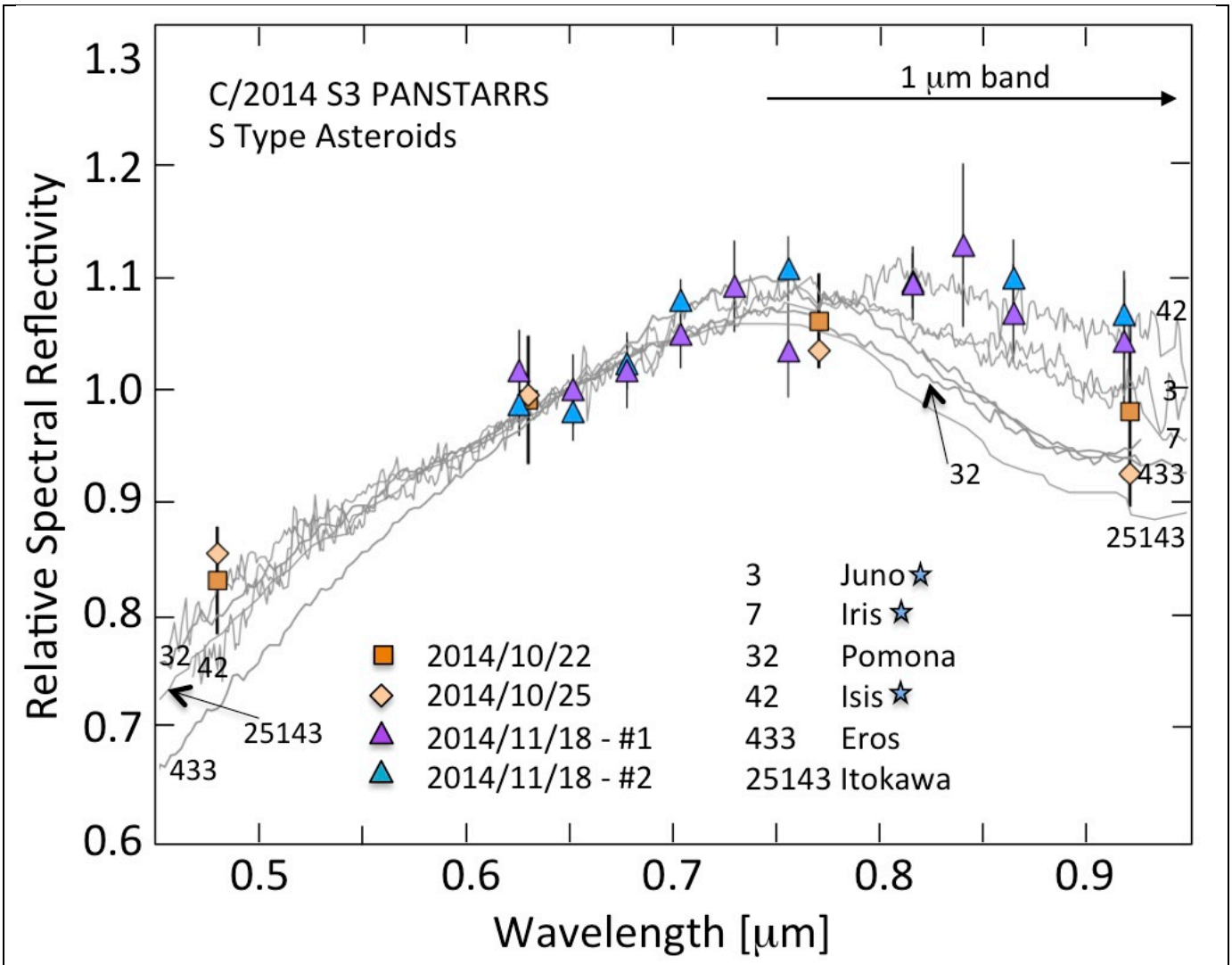

Figure 2. CFHT photometry converted to spectral reflectivity obtained on UT 2014 October 22 and 25 is shown in comparison to the VLT reflectivity spectrum obtained on UT 2014 November 18. Data beyond 0.9μm were affected by bright night sky emission lines that could not be satisfactorily subtracted; they are included for comparison with the CFHT data. Two independent methods were used to process the spectra (#1, #2). The spectra have been binned to increase the signal to noise. The location of the 1 μm band characteristic of S-type asteroids is shown, and the spectra of six S-type asteroids with a shallow 1 μm feature are shown for comparison (*24,35*); the star symbols denote the S(IV) type asteroids. All spectra are normalized to 0.65 μm. The data for C/2014 S3 are consistent with these S-type asteroids.

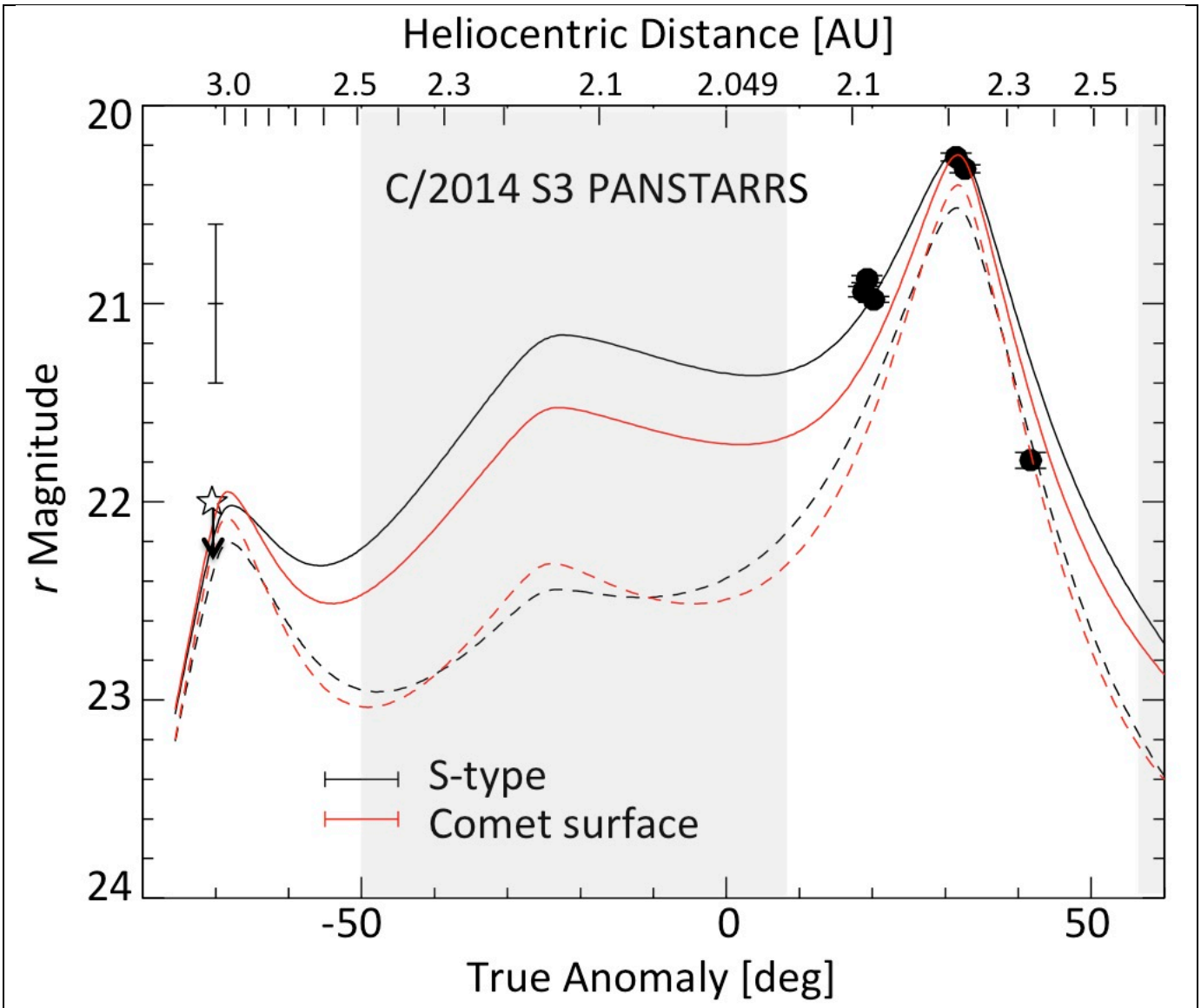

Figure 3. Water ice sublimation models compared to measured *r*-band brightness as a function of position along the orbit (TA=true anomaly; TA=0^{o} is at perihelion). The solid line shows the total brightness contribution from the nucleus and the dust, and the dashed line shows the contribution from the nucleus only. Models for a low-albedo comet nucleus surface and a brighter S-type asteroid surface are shown. By TA=41.7^{o} the activity had significantly decreased. No combination of nucleus size and activity level can reproduce all the data without assuming a decrease in activity; the best fit is presented. The error bar-like symbol at TA=-70^{o} shows a possible maximum rotational brightness amplitude. The star symbol shows an upper limiting magnitude from searching the Pan-STARRS1 database for pre-discovery images. The grey shading indicates times when C/2014 S3 was not observable because it was in solar conjunction.

Supplementary Information

Meech, et al.

Supplementary Methods

S1. Details of the Observations

A log of the observing dates, orbital geometry, and observing conditions is shown in Table S1. All the imaging data were obtained in the Sloan *gri* filter system (*36*).

After it became clear that C/2014 S3 was very interesting, on 2014 Nov. 14 our team requested Director's discretionary time on the European Southern Observatory (ESO) Very Large Telescope to obtain a spectrum and within 5 hours we received a positive answer. Concerned about the potential target faintness, we obtained observations on UT 2014 Nov. 16 using the Megaprime mosaic camera on the CFHT. This showed that the comet had rapidly faded and was a magnitude fainter than predicted.

Optical spectra were obtained using the VLT FOcal Reducer and low dispersion Spectrograph (FORS2) on the UT1 telescope two nights later, on 2014 Nov. 18. We used the GRIS300I+11 grism with the OG590 filter. This combination provided the highest transmission between 0.8-0.9 μm for a total wavelength range from 0.45-0.95 μm. We used a 1.0×408 arcsec slit that provided a spectral resolving power of 600 at $\lambda_{central}$ = 0.858 μm. To correct for strong telluric absorption features from the atmosphere, we observed the G2V star HD224817, which was close to C/2014 S3 in the sky. This star also served as a solar analog for determining reflectivity.

S2. Data Reduction

S2.1. Image Data Reduction

The imaging data was calibrated using field stars belonging to the PSPS export database (*37*). We converted the Pan-STARRS1 3pi mean psf magnitudes to SDSS AB magnitudes using the transformations in (*38*). Image photometry was performed using the SExtractor package (*39*). SExtractor automatic aperture photometry (MAG_AUTO) with expanded apertures was used for trailed or crowded images; for most non-trailed images a curve of growth was developed using a series of sextractor aperture magnitudes. Final object photometry was performed using the same method (MAG_AUTO or aperture) used to calibrate the image. The spectral reflectivities were computed from the photometry using the following formula:

$$S'(\lambda) = 10^{-0.4[m(\lambda)-m(\lambda,\odot)]} / 10^{-0.4[m(\lambda)-m(g,\odot)]} \quad [1]$$

Here m(⊙) is the magnitude of the sun at the specific filter wavelength, λ, with the spectral reflectivity normalized to a value of 1 in the *g* filter. The colors for the sun in the *griz* system are: m(*g,*⊙) - m(*r,*⊙) = 0.44±0.02, m(*r,*⊙) - m(*i,*⊙) = 0.11±0.02, m(*i,*⊙) - m(*z,*⊙) = 0.03±0.02 (*40*).

S2.2. Spectral Data Reduction

Because of the low contrast between the bright sky and faint object, we performed two independent reductions.

Reduction 1 – Nominal data processes (i.e. bias subtraction, flat fielding and wavelength calibration) were performed using the FORS2 pipeline with Gasgano (a Data File Organiser developed and maintained by the European Southern Observatory). The first order sky removal was performed as part of the FORS2 pipeline procedure. Additional skyline removal and the extraction of one-dimensional spectra of the comet as well as the standard star were carried out using standard IRAF tasks.

Reduction 2 – The spectra were extracted in a stepwise fashion to account for the curvature in the *y*-direction of the spectrum dispersed along the *x*-direction on the CCD. The extraction box size was 9 pixels wide. The same size box is used for sampling the sky both above and below the spectrum. The sky values from the top and bottom sky are cross-correlated to see if there is any shift in the lines; there were none. We used the average of the two sky regions to subtract the sky from each of the four target spectra. We deleted the cosmic rays by linearly interpolating across them. Then the four spectra were averaged together. We used an identical procedure to process the solar-like standard star, with the exception that the extraction box width was 11 pixels. We divided the Manx spectrum by the solar standard spectrum to get the reflectivity.

The spectra have been binned into intervals representing the regions free of night sky emission lines to increase the signal-to-noise.

S3. Solar System Formation Model Predictions

In this section we briefly summarize the models that we refer to in the main text and their predictions in terms of asteroidal mass in the Oort cloud.

S3.1 The Grand Tack model

In this model (*1*), Jupiter starts to form at the snowline, near 3.5 AU. It migrates inwards while Saturn is still growing. When Jupiter reaches a distance of ~1.5 AU, Saturn achieves a mass large enough to influence the migration of Jupiter. Jupiter reverses migration direction (*41*) and the two giant planets start to migrate outwards until Jupiter reaches a final distance of ~5.4 AU.

During the inward migration phase, Jupiter and its resonances sweep approximately two Earth masses (M⊕) of material that was originally inside of it's orbit. The material in this region was likely volatile-poor (represented in today's meteorites by ordinary chondrites, enstatite chondrites, and differentiated planetesimals). The parent bodies of these volatile-poor meteorites are the S-type

asteroids (*23*). Of these 2M⊕ of S-type material, 14% is scattered outward, ending up beyond 3 AU. When the planets migrated outwards they again encountered this scattered material. About 5% of this is implanted in the asteroid belt, and 13% survives beyond Neptune. This represents a total of 0.14 × 0.13 × 2 = 0.04 M⊕ of S-type material mixing with the local disk of comets. Later, when the giant planets became unstable and the cometary disk was dispersed (*42*), this inner-disk material followed the same dynamical fate of the comets. About 5% of it ends in the Oort cloud and 1% in the scattered disk. So today, there should be about 0.002M⊕ of S-type material in the Oort cloud (compared to 1-2 M⊕ of comets (*43*) and 0.0004M⊕ of S-type material in the scattered disk (compared to 0.3 M⊕ of comets (*43*)). In other words, the Grand Tack model predicts that the ratio of icy comets to S-type material in cometary orbits should be about 500-1000 to 1. Notice that the bodies ejected during the Grand Tack events (i.e. those which do not end up in the trans-Neptunian disk but are expelled into orbits with a > 1000 AU or even hyperbolic orbits) are unlikely to contribute to the build-up of the Oort cloud. This is because this event occurred very early (the first few My of the Solar System history, before the removal of the protoplanetary disk), so that the Sun was likely still embedded in a stellar cluster. In presence of a cluster, the orbits of the distant objects bound to the Sun are not typical of the Oort cloud, but are similar to that of Sedna (*44,45*). This issue is less critical for the other models described below, because the planetesimals are scattered to distant orbits at a later time (typically during terrestrial planet formation, which took several tens of My), so that the Sun might have already escaped from its birth cluster.

S3.2 The Shannon et al. (2015) model

This model is a fairly simple one, in which all planets are assumed to be fully formed on their current orbits; test particles are distributed uniformly through the Solar System and their evolution is simulated until their ultimate dynamical removal or the age of the Solar System is attained (*3*). Somewhat less than 1% of the test particles from the terrestrial planet region are found to reach the Oort cloud. In these simulations, the asteroid belt is stable, so its test particles do not escape and do not contribute to the Oort cloud. In order to estimate the fraction of the Oort cloud population represented by inner Solar System planetesimals, Shannon et al. assume that the initial planetesimal surface density distribution follows $1/r^{3/2}$ law characteristic of the Minimum Mass Solar Nebula model (*46*). With this assumption, they find that 4% of the Oort cloud objects should come from the inner Solar System, almost all of which from within 2 AU from the Sun. However, the assumption that the surface density of planetesimals at the end of terrestrial planet formation followed a $1/r^{3/2}$ law neglects that part of this mass should have been used to build the terrestrial planets in first place. Thus, we can improve this estimate as follows. In Shannon et al., about 20% of the planetesimals in the terrestrial planet region hit the Earth. We know from geochemistry of the Earth mantle that our planet accreted only ~1% of its own mass as a late Veneer (*47*). Thus, the total mass of planetesimals in the terrestrial planet region should have been of the order of 0.05 M⊕. If we apply now a 1% efficiency of implantation in the Oort cloud we conclude that at most 1/2000 of the Oort cloud population (assumed to be 1 Earth mass) should come from the inner Solar System.

S3.3 The Izidoro et al. (2013) Depleted Disk model.

This model simulates the formation of the terrestrial planets from a disk of planetesimals and planetary embryos (*5*). There are initially 2 M⊕ of planetesimals, between 2.5 and 4 AU. Jupiter and Saturn are assumed to be fully formed and on their current orbits. In some simulations only Jupiter is considered. Most of the planetesimals (~1.7 M⊕) are dynamically removed during the simulation. Their fate is not explicitly discussed in the paper. But assuming that 50% of them suffer close encounters with Jupiter (typical of asteroid belt depletion simulations; the rest falling into the Sun or being accreted by the terrestrial planets) and that 1% of these is emplaced in the Oort cloud (as in Shannon et al.), we expect that this model produces about 0.01 M⊕ of asteroidal material in the Oort cloud of which roughly half would be S-type objects. Compared to the total mass of the Oort cloud (1-2 M⊕), this implies that the ratio icy objects/S-type objects in the cloud is 200-400.

S3.4 The Weissman and Levison (1997) estimate

It this work the authors assumed that the primordial mass of the asteroid belt was ~3 M⊕ and that during the primordial depletion of the asteroid belt half of this material was removed by encounters with Jupiter (*4*). They also assumed that 8% of the population encountering Jupiter ends in the Oort cloud. This amounts to 0.12 M⊕ of asteroidal material in the Oort Cloud, about half of which is in S-type bodies. Using a modern estimate for the Oort cloud mass of 1-2 M⊕ (*43*), then 3-6% of the Oort cloud objects should be S-type objects (the authors assumed an Oort Cloud mass of 16 M⊕, concluding that 1% of it should be asteroidal). However, they admitted that the 8% implantation efficiency into the Oort cloud came from numerical simulations which "did not include the effects of galactic tides or passing stars and thus should be considered preliminary". A refined estimate for the implantation efficiency is ~1% (*3,48*), so the revised expectations from Weissman and Levison (4) should be in line with those from the model of Izidoro et al. (*5*)

S3.5 The Levison et al. (2015) Pebble Accretion Model

The goal of this model (*6*) is to provide a solution to the problem of the small mass of Mars without invoking a wide range migration of Jupiter as in the Grand Tack scenario (*1*). It is assumed that planetary embryos grow due to a very efficient process known as "pebble accretion" (*49*). A few drastic assumptions are made on the protoplanetary disk structure. First, that the disk is assumed to be flared also in its inner part, which requires a radial gradient in the dust/gas ratio. Second, it is assumed that the disk exhibits a pressure bump at the snowline, so that there is no pebble drift into the inner disk from the outer disk. Consequently, the planetary embryos in the inner disk grow only from pebbles that form by condensation and coagulation within the snowline. With these assumptions, accretion is strongly favored closer to the Sun than farther out. The population of planetesimals initially in the asteroid belt does not grow in mass significantly, whereas the planetesimals in the terrestrial planet region grow much more effectively and become planetary embryos. In this way, the resulting mass distribution is strongly concentrated within 1 AU, which leads to the formation of a massive Earth and of a much less massive Mars (*50*). A characteristic of the pebble accretion model is that the small body populations are never massive, accounting in total less than 1% M⊕. Thus, the total amount implanted in the Oort cloud is at most 10^{-4} M⊕, thus predicting a ratio of icy/rocky bodies in the cloud larger than 10,000.

Basically, we can conclude that all models assuming primordial massive populations of small bodies in the inner Solar System, regardless of the specific aspects of planet evolution, expect an icy/S-type ratio in the Oort cloud of several hundreds to 2,000, whereas the new model suggesting that the asteroid belt always had a very low mass implies a ratio larger than 10,000.

S4. **Conceptual Ice Sublimation Model**

We use a simple ice-sublimation model (*51*) to investigate the origin of the dust coma for C/2014 S3. This model was used to investigate the behavior of comet 67P/Churyumov Gerisamenko prior to arriving at the comet, and successfully predicted the gas flux levels when the Rosetta spacecraft first started to detect gas (*52*). The model computes the amount of gas sublimating from an icy surface exposed to solar heating. The brightness of a bare nucleus is related to its radius, R_N [m], and geometric albedo, p_λ, by:

$$p_\lambda R^2_N = 2.235\times10^{22}\ r^2\ \Delta^2\ 10^{[0.4(m(\odot)\ -\ m)]}\ 10^{0.4(\beta\alpha)} \qquad [2]$$

where r and Δ are the helio- and geocentric distances [AU] and $m(\odot)$ and m are the apparent magnitudes of the sun and comet. The term $\beta\alpha$ represents the simplified linear phase function, with phase angle, α [deg] and β is a constant ranging from 0.02-0.04 mag / degree.

As the ice sublimates, either from the nucleus surface or near subsurface, the escaping gas entrains dust in the flow, which escapes into the coma and tail thus increasing the effective cross section for scattered light. This is observed as a brightening in the heliocentric light curve, which can be compared to observed photometry. In the absence of gas fluorescence, the total comet brightness has a contribution from the nucleus and the scattered light from the dust. The latter is proportional to the total dust cross section, $p_\lambda R_{dust}$, where R_{dust} is the radius of a disk of cross section equal to the total grain cross section. This can be related to a coma brightness using a variant of Eq. (2). Assuming uniform mass loss from the nucleus, the total mass of grains within a projected photometry aperture is a product of the mass loss rate times the time spent in the aperture. This is related to the total grain cross section in an optically thin coma. The total coma brightness can be expressed as a function of mass loss via:

$$m_{coma} = 30.7 - 2.5\ \log10\ [\ p_\lambda\ (dM/dt)\ t\ /\ \rho\ a\ r^2\ \Delta^2\ ] \qquad [3]$$

where the time, t, is a function of the projected aperture size and grain velocity and a and ρ are the grain radius and density, respectively. The mass loss is computed using the energy balance at the nucleus:

$$F_\odot\ (1 - A)\ /\ r^2 = \chi\ [\varepsilon\ \sigma\ T^4 + L(T)\ (dm_s/dt) + \kappa(dT/dz)] \qquad [4]$$

The left side of the equation is the incident solar flux, $F_\odot$, absorbed (where A is the bond albedo), which is partitioned into blackbody energy, sublimation and conduction into the interior. The term χ is related to the rotation-modulated distribution of incident solar energy; ε is thermal emissivity (ε=0.9), and T is the temperature. The mass loss per unit area, (dm_s/dt) is related to the sublimation vapor

pressure *P(T)* and the average speed of the gas molecules leaving the surface; *L(T*) is the latent heat of sublimation (*53*). The thermal conductivity, κ, is known to be low (*54*).

The model free parameters are: ice type, nucleus radius, albedo, emissivity, density, dust sizes, density, phase function, thermal conductivity and fractional active area. Because we had very few distinct data points, we did not allow all the variables to vary independently. Rather, we ran models for water ice for an S-type asteroid (25% albedo, density 3000 kg m^{-3}, phase function 0.03 mag/deg) and a typical comet (4% albedo, density 400 kg m^{-3}, phase function 0.04 mag/deg). We further assumed a slow rotation, and small micron-sized grains. The S-type model was best fit with a nucleus radius of 0.26 km and the comet model with a nucleus of 0.71 km. The inferred fractional active area was small, with satisfactory fits for 0.04% to 0.1% of the body's total area, and the inferred gas production rate was around 10^{23}-10^{24} molecules s^{-1}.

S5. Finson Probstein Dust Models

In order to investigate the morphology of C/2014 S3's coma, we used the Finson-Probstein method (*55*), which considers dust grains released from the nucleus with zero velocity, at various epochs in the past, and computes their position at the time of the observations accounting only for the solar radiation pressure and gravity. The ratio between these two forces is a function of the size and density of the dust grains, and of the radiation pressure efficiency. We used a density of 3000 kg m^{-3} (typical for S-type asteroids, (*56*)), and the particle size was set to scan the range from 1 to 1000 μm. All the grains released at a given epoch will have spread over a line connecting the nucleus (representing a giant particle unaffected by radiation pressure) to the smallest grains, forming a "synchrone" line. The line connecting the dust grains of a given size emitted at various epochs is a "syndyne'".

Syndynes and synchrones often form a very narrow fan, and the various epochs and sizes degenerate into a single inextricable line. Observationally, this corresponds to the typical long and narrow tail of a comet. Fortunately, during 2014 Sep. and Oct., the viewing geometry of the comet was very favorable, with the syndynes and synchrones broadly fanning out. In the ideal case where the dust is emitted with negligible velocity and the comet observed with superb image quality, overlaying the syndynes and synchrones on the image of the comet allows us to directly read the emission time and the grain size for any pixel of the image. The atmospheric turbulence blurs the images, and the gas resulting from the ice sublimation driving the cometary activity can push the dust grains out with a high velocity. Because of both these effects, the syndynes and synchrones cannot be used directly, but are still useful to guide the analysis of the images. Conversely, the presence of dust outside the region covered by the curves unequivocally indicates that the dust must have been released with some velocity.

S6. Statistical Assessment: Manx Observations and Dynamical Models

We use a statistical basis to determine how many Manx objects need to be observed in order to discriminate between the dynamical models which make different predictions for the amount of inner solar system S-type material that should be in the Oort cloud.

We assume four competing models with S-type fractions of A) 0.01% B) 0.05%, C) 0.13%, and D) 0.33%. We further assume that destruction of LPCs leads to a 13-fold suppression of LPCs in the in-scattered sample **(***57***).** Then, we note that our observational definition of a Manx selects only those objects on long-period comet orbits that are inactive or nearly inactive. Assuming that pre-selecting for low-activity objects will increase the fraction of S-types in the sample by a factor of three over randomly chosen Oort-cloud objects (based on recent active LP comet discoveries compared to Manx discoveries), we obtain a total enhancement of 3×13=39 of S-types over the above Oort cloud S-type fraction for each model.

We then use cumulative binomial statistics to examine which models are ruled out at a 2-sigma level given a particular observed number of S-types. If we observe 10 Manx objects, we can rule out hypothesis A if among them we see even a single S-type, B if we see two or more, C if we see three or more, and D if we see four or more. If we manage to observe 100 Manx objects, we can then rule out C if we do not see between 2 and 9 S-types; and D if we do not see between 8 and 19. It is important to note that even in regions where competing hypotheses are permitted at the 2-sigma level, it is still possible to assign relative likelihoods.

Table S1 – Observing Circumstances

Tel[a]	UT Date	Start UT	JD[b]	*r*[c]	Δ[c]	α[c]	TA[c]	Fil[d]	#[e]	t[e]	*Mag*[f]	σ[f]	Refl[g]	σ[g]
Imaging - Photometry														
CFHT	2014/09/23	14:56:36	6924.122645	2.106	1.543	26.61	19.2	r	3	180	20.941	0.028		
CFHT	2014/09/24	15:02:31	6925.126751	2.110	1.522	26.23	19.6	r	2	300	21.026	0.025		
CFHT	2014/09/26	13:59:04	6927.082686	2.115	1.484	25.39	20.4	r	4	720	20.979	0.015		
CFHT	2014/10/22	12:52:42	6953.036593	2.210	1.227	5.27	31.5	g	3	180	20.861	0.033	1.00	0.042
CFHT	2014/10/22	12:38:34	6953.026786	2.210	1.227	5.27	31.5	r	3	180	20.261	0.021	1.16	0.048
CFHT	2014/10/22	12:45:48	6953.031806	2.210	1.227	5.27	31.5	i	3	180	20.082	0.024	1.23	0.057
CFHT	2014/10/22	12:59:31	6953.041331	2.210	1.227	5.26	31.5	z	2	120	20.193	0.062	1.15	0.085
CFHT	2014/10/24	12:32:30	6956.022566	2.224	1.240	5.07	32.7	g	3	180	20.892	0.026	1.00	0.034
CFHT	2014/10/24	12:40:15	6956.027951	2.224	1.240	5.07	32.7	r	3	180	20.892	0.026	1.14	0.041
CFHT	2014/10/24	12:47:27	6956.032959	2.224	1.240	5.07	32.7	i	3	180	20.163	0.031	1.18	0.052
CFHT	2014/10/24	12:57:25	6956.039868	2.224	1.240	5.07	32.7	z	5	400	20.294	0.035	1.07	0.046
CFHT	2014/11/16	05:26;10	6977.726500	2.332	1.588	19.48	41.0	r	1	120	22.23	0.16		
VLT	2014/11/18	01:37:08	6979.567454	2.343	1.632	20.25	41.7	r	2	120	21.786	0.040		
Spectroscopy														
VLT	2014/11/18	02:18:16	6979.596013	2.343	1.632	20.26	41.7	h	4	3600				

[a] Telescope: CFHT=Canada-France-Hawaii 3.8m, VLT=Very Large Telescope 8.0m

[b] JD-24500000 at start of observation.

[c] Heliocentric, geocentric distances [AU], solar phase angle [deg], and true anomaly [deg].

[d] Filter ($\lambda_{Central}/\Delta\lambda$ [μm]: g (0.475/0.154), r (0.640/0.148), i(0.776/0.155), z (0.925/0.153)) or grism.

[e] Number of exposures, and total exposure time [sec].

[f] *r* mag and error.

[g] Spectral reflectivity normalized to a value of 1 at λ=0.65 μm and error.

[h] 300I+OG590